Acta Materialia 171 (2019) 65–78

Contents lists available at ScienceDirect

Acta Materialia

journal homepage: www.elsevier.com/locate/actamat

Full length article

Transitory phase transformations during $\{10\bar{1}2\}$ twinning in titanium

Peng Chen [a, b], Fangxi Wang [a, b], Bin Li [a, b, *]

[a] Department of Chemical and Materials Engineering, University of Nevada, Reno, USA
[b] Nevada Institute for Sustainability, University of Nevada, Reno, USA

ARTICLE INFO

Article history:
Received 26 December 2018
Received in revised form
22 February 2019
Accepted 1 April 2019
Available online 9 April 2019

Keywords:
Titanium
Phase transformation
Twinning

ABSTRACT

$\left\{10\bar{1}2\right\}\left\langle10\bar{1}\bar{1}\right\rangle$ twinning presents a variety of properties that entirely depart from the classical twinning behavior. In this work, deformation of a single crystal Ti under uniaxial compression perpendicular to the *c*-axis was investigated by using atomistic simulations. Very interesting phase transformations between body centered cubic (BCC), hexagonal close-packed (HCP), face centered cubic (FCC) structures were observed. These phase transformations are only transitory. Before twin nucleation, $HCP_{parent} \rightarrow BCC$ transformation occurred. The lattice transformation can be described as: $(10\bar{1}0)_P \rightarrow (110)_{BCC}$, and $(0002)_P \rightarrow (1\bar{1}0)_{BCC}$. Then the BCC phase transformed to HCP which satisfies $\left\{10\bar{1}2\right\}\left\langle10\bar{1}\bar{1}\right\rangle$ twin relationship with the HCP parent. This transformation is accomplished by atomic shuffles and no shear is involved. After the BCC phase was entirely transformed, the deformation was dominated by twin growth. At the twin boundary (TB), a FCC phase was present, separating the parent from the twin. The FCC structure was transformed from the HCP parent. This transformation is also transitory and involves both shear and shuffle. Shuffling transforms the double-layered $(10\bar{1}0)_P$ plane of parent into a close-packed $(111)_{FCC}$ plane, and then a shear with a Burgers vector of half a Shockley partial dislocation on the $(111)_{FCC}$ plane generates the correct FCC structure. It was observed that the formation of FCC phase at the TB hinders twin growth. But as the strain increases, the FCC phase transformed to the HCP twin and this process involves Shockley partials on the interface. Strain accommodation was analyzed to explain the formation of the FCC phase at the TB. These transitory phase transformations during deformation twinning further corroborate that $\left\{10\bar{1}2\right\}\left\langle10\bar{1}\bar{1}\right\rangle$ twinning completely departs from the classical twinning behavior.

1. Introduction

In plastic deformation of hexagonal closed-packed (HCP) metals (e.g. Ti, Co, Zr and Mg), deformation twinning plays a crucial role in the mechanical behavior of this important class of engineering materials [1–6]. Among all the twinning modes that were well predicted and described by classical twinning theory [1], $\left\{10\bar{1}2\right\}\left\langle10\bar{1}\bar{1}\right\rangle$ twinning is the most important and has been extensively observed and discussed in both experimental and simulation studies [7–10]. The most salient feature of this particular twinning mode is its departure from the classical twinning behavior. Twinning in metals with cubic crystal structures is always mediated by well-defined twinning dislocations which are partial dislocation and strictly glide on the twinning plane [11–13]. For other twinning modes than $\{10\bar{1}2\}$ in HCP metals, similar classical behavior has been observed [1,14–16], with a major difference being that the twinning dislocations are "zonal twinning dislocations" involving two or more twinning planes simultaneously [1,14,16]. In sharp contrast, $\{10\bar{1}2\}$ mode presents a variety of non-classical properties that challenge the descriptions of the classical theory [17–21]. In early 1960s, using optical microscopy, Partridge et al. [22] observed that a $\{10\bar{1}2\}$ twin boundary (TB) in pure Mg evolved into "extremely" incoherent structures, i.e. bulging in or out, when a hardness indenter tapped into the material at the vicinity of the TB. They estimated that, if there were "twinning dislocations" on the incoherent TBs, the spacing between the twinning dislocations would be 0.4–0.5 nm which is impossibly small.

* Corresponding author. Department of Chemical and Materials Engineering, University of Nevada, Reno, USA.
E-mail address: binl@unr.edu (B. Li).

https://doi.org/10.1016/j.actamat.2019.04.002
1359-6454/

Abnormal properties of $\{10\bar{1}2\}$ twinning were later observed by Gharghouri et al. [23] by using transmission electron microscopy (TEM). They found that a $\{10\bar{1}2\}$ twin variant can change its habit plane when it encounters and interacts with a precipitate and the variant can entirely engulf the precipitate without being stopped during twin growth. Using in-situ TEM, Liu et al. [24] observed that a $\{10\bar{1}2\}$ twin can grow without producing any shear strain on a single crystal specimen of Mg. TEM studies of TB structure also showed that $\{10\bar{1}2\}$ TBs may entirely deviate from the theoretical twinning plane by very large angles (tens of degrees) [18,25]. Consistent with these experimental observations, numerous atomistic simulations of $\{10\bar{1}2\}$ twin growth showed that migrating TBs are mostly incoherent [8,17,26]. This abnormal behavior led Serra et al. [27] to the proposition of "twinning disconnections" on the TBs. However, this concept cannot explain why only this particular twinning mode departs from the classical behavior, whereas other twinning modes generally closely follow the descriptions of the classical theory.

Another highly abnormal phenomenon is the presence of face centered cubic (FCC) phase at $\{10\bar{1}2\}$ TBs, as reported in most recent studies [28,29]. Ren et al. [28] observed the transformation from HCP to FCC at a $\{10\bar{1}2\}$ TB in deformation of single crystal Ti in their atomistic simulations. Hirth et al. [29] also reported that an FCC phase was generated at a $\{10\bar{1}2\}$ TB and the FCC phase was eventually sandwiched in between the parent and $\{10\bar{1}2\}$ twin. They suggested that the FCC phase was formed by "disconnections" at TBs. However, no detailed analyses were provided in these works. Questions such as how the FCC phase is actually formed at the TBs and how it interacts with TB migration remain unclear. Also, the orientation relationship (OR) between the FCC, HCP parent and HCP twin was not analyzed in these reports.

In this work, atomistic simulation of uniaxial compression on a Ti single crystal perpendicular to the *c*-axis was performed. Surprisingly, BCC and FCC transitory phases were observed in activation of $\{10\bar{1}2\}$ twinning. The OR between multiple phases was carefully analyzed and the underlying mechanisms for the phase transformations were investigated. Energetics of the phase transformations and their influence on TB migration was calculated. This work provides new insight in phase transformations initiated in plastic deformation of HCP metals.

2. Simulation method

The embedded atom method (EAM) potential [30,31] for Ti–Al binary system developed by Zope and Mishin [32] was used in this work. This potential has been used in a number of atomistic simulations of deformation of Ti and Ti alloys [16,33]. The initial configuration is shown in Fig. 1. A single crystal of Ti was first constructed with a dimension of $25 \times 25 \times 25\ \text{nm}^3$, containing a total of about one million atoms. Free surfaces were applied to all three dimensions. Periodic boundary condition was not used in this work because undesirable local stresses can be generated from the interaction between atoms on opposite boundaries. To track the structural evolution during deformation, the basal planes of the Ti crystal are colored alternately in red and blue, such that the … *ABABAB* … HCP stacking sequence is revealed. To identify the lattice transformation during structural evolution, five prismatic planes of the crystal were pre-selected and colored differently. The color pattern of the whole system was retained during simulation and this allows one to unambiguously analyze to what planes these pre-selected planes were transformed. This step is crucially important for analyzing the deformation mechanisms with clarity.

The system was fully relaxed before an external compression

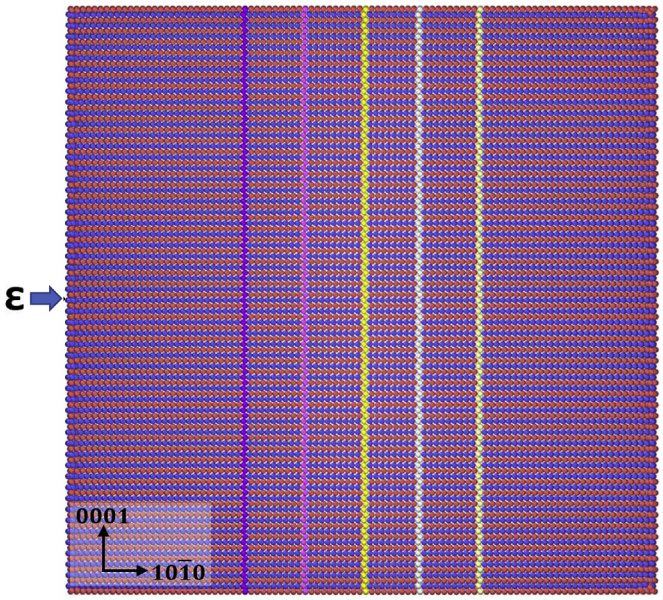

Fig. 1. Initial configuration of the simulation for a single crystal of titanium. The basal planes were colored alternately to show the … ABABAB … stacking sequence. Five prismatic planes were pre-selected and colored differently to track the lattice transformation. A compressive load was applied along the $[10\bar{1}0]$ direction.

strain was applied along the $[10\bar{1}0]$ direction of the crystal. The compressive strain was generated by moving the atoms on the left free surface towards right at a constant displacement rate of 0.01 nm per femtosecond, corresponding to a strain rate of 4.0×10^{11}/sec. The temperature was maintained at 100 K during simulation. Free surfaces were applied to all three dimensions. The visualization tool Ovito [34] was used to analyze the simulation results. Common neighbor analysis (CNA) [35] was used to distinguish the crystal structures and lattice defects.

To examine the energies of different phases, the density-functional theory (DFT) calculation was performed with Vienna Ab-initio Simulation Package (VASP) [36–38]. The Projector Augmented Wave (PAW) [39,40] and the Generalized Gradient Approximation of Perdew-Burke-Ernzerhof (GGA-PBE) [41] were applied. The $3d^3 4s^1$ electronic configuration of titanium was the valence state for the PAW pseudopotential. The total energy cutoff was 600 eV. A Monkhorst-pack $13 \times 13 \times 13$ mesh was used, and the electronic self-consistent field was set at 10^{-6} eV/Å.

3. Results

Transformation from HCP parent to BCC phase in time sequence is displayed in Fig. 2. In the CNA, atoms in the HCP parent are shown in red, whereas those atoms in the BCC phase are shown in blue. Although the compressive load was applied along the $[10\bar{1}0]_P$ of the parent crystal and such a loading condition favors $\{10\bar{1}2\}$ extension twinning, the BCC phase was first nucleated before the activation of extension twinning (Fig. 2a), as the compressive strain was increased to a threshold value. The BCC phase was nucleated near the top and bottom free surface, as well as in the interior of the parent. As the compressive strain increases, the BCC phase grows at the expense of the HCP parent (Fig. 2b). It can also be seen that the interface between the HCP parent and the BCC phase is highly irregular and incoherent. As the strain further increased, the BCC phase continued to grow, and eventually the middle section of the parent was transformed into the BCC structure. It is noted that the HCP to BCC phase transformation creates a slight contraction

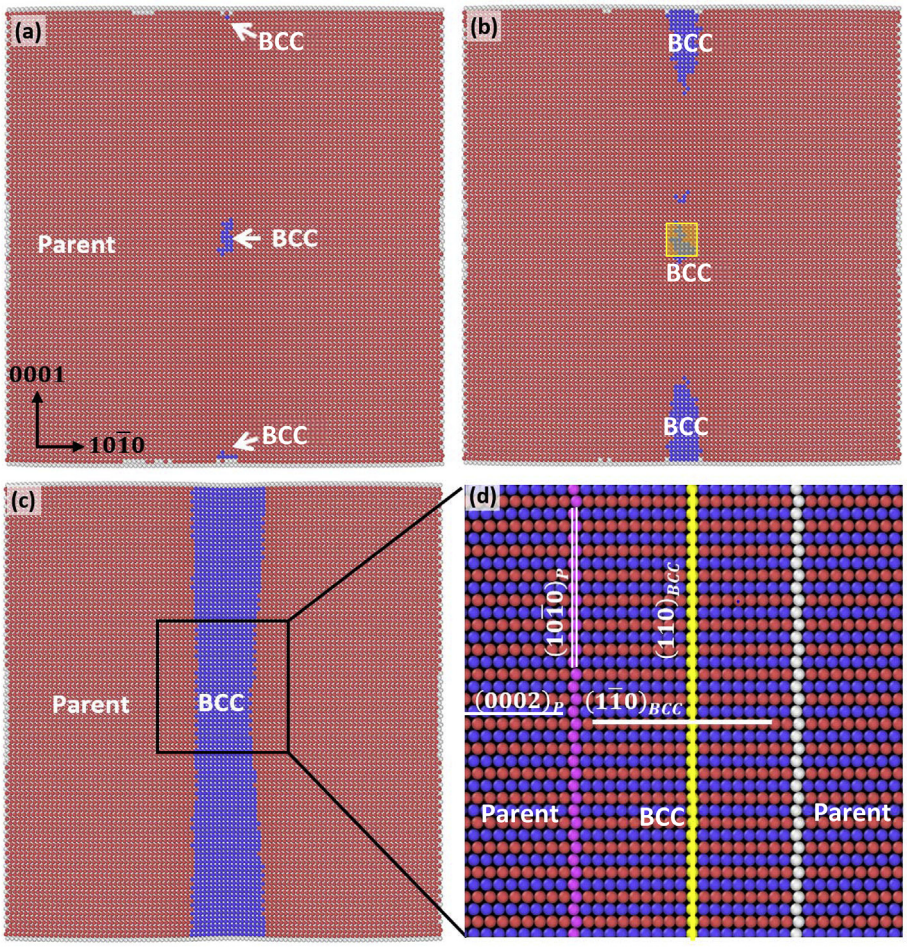

Fig. 2. (a)–(c) Common neighbor analysis (CNA) of transformation from HCP parent (in red) to BCC (in blue) in time sequence. (a) Nucleation of BCC near the surface and the center. (b) Growth of the BCC inside the parent. The boxed region is selected to compute the energy evolution. (c) As the strain increases, the BCC continues to grow. (d) Magnified view of the boxed region in (c) without CNA. After transformation the double-layered $(10\bar{1}0)_P$ prismatic of the parent was transformed to single-layered close-packed planes $(110)_{BCC}$ of the BCC. In this orientation relationship, $(0002)_P \parallel (1\bar{1}0)_{BCC}$. (For interpretation of the references to color in this figure legend, the reader is referred to the Web version of this article.)

perpendicular to the loading direction, as manifested at the top and bottom surfaces (Fig. 2c). A slight extension is also created in the $[1\bar{2}10]$ direction (not shown).

To track the structural evolution during deformation and phase transformation, the boxed region in Fig. 2c is magnified and analyzed in Fig. 2d. In this plot, the CNA is turned off, so all the atoms have the originally assigned colors, irrespective of the crystal structure of phases. This helps identify the lattice transformation and the orientation relationship. It can be readily seen that, in the BCC region, the originally corrugated, double-layered yellow prismatic plane of the parent, i.e. the $(10\bar{1}0)_P$, has transformed to a flat, single-layered $(110)_{BCC}$ of the BCC phase, whereas the originally flat basal plane of the parent has now transformed to the $(1\bar{1}0)_{BCC}$ of the BCC phase. Thus, the lattice transformation can be described as: $(10\bar{1}0)_P \rightarrow (110)_{BCC}$, and $(0002)_P \rightarrow (1\bar{1}0)_{BCC}$. The orientation relationship between the HCP parent and the BCC phase can be described as: $(0002)_P \parallel (1\bar{1}0)_{BCC}$, $(10\bar{1}0)_P \parallel (110)_{BCC}$. This orientation relationship is essentially identical to the reports in the literature [42–44].

As the compressive strain further increased to a critical value, the BCC phase started to transform into HCP. However, as analyzed below, the newly formed HCP is 90° away from the HCP parent around the zone axis of $\langle 1\bar{2}10 \rangle$, and this misorientation satisfies $\{10\bar{1}2\}\langle 10\bar{1}\bar{1} \rangle$ twin relationship, although the theoretical misorientation equals 85°. Why these two HCP phases are $\{10\bar{1}2\}$ twins is demonstrated in Appendix. The transformation process is shown in Fig. 3. The HCP phase emerges in the central region of the BCC phase (Fig. 3a). In the CNA analysis, both the HCP parent and the HCP twin are colored in red, The HCP twin continues to grow by consuming the BCC phase as the deformation proceeds (Fig. 3b). The interface between the BCC phase and the HCP twin is irregular and incoherent. In Fig. 3c, the HCP twin continues growing at the expense of the BCC phase. Note the interface appears to be a circular shape in 2D view, indicating that the habit plane is not well defined. After the two thin walls of BCC are consumed, the HCP twin and the HCP parent become in contact. To examine the orientation relationship between the newly formed HCP twin with respect to the HCP parent and the BCC phase, the boxed region in Fig. 3b is magnified and further analyzed in Fig. 3d. Compared to the HCP parent, the $(0002)_P$ basal planes of the parent are parallel to the $(10\bar{1}0)_T$ prismatic plane of the newly formed HCP twin and vice versa. The newly formed HCP and the original HCP parent satisfies $\{10\bar{1}2\}$ twin relationship, i.e. $90°\langle 1\bar{2}10 \rangle$. It can also be observed that the single-layered $(1\bar{1}0)_{BCC}$ planes of the BCC phase are transformed to the double-layered $(10\bar{1}0)_T$ prismatic plane of the

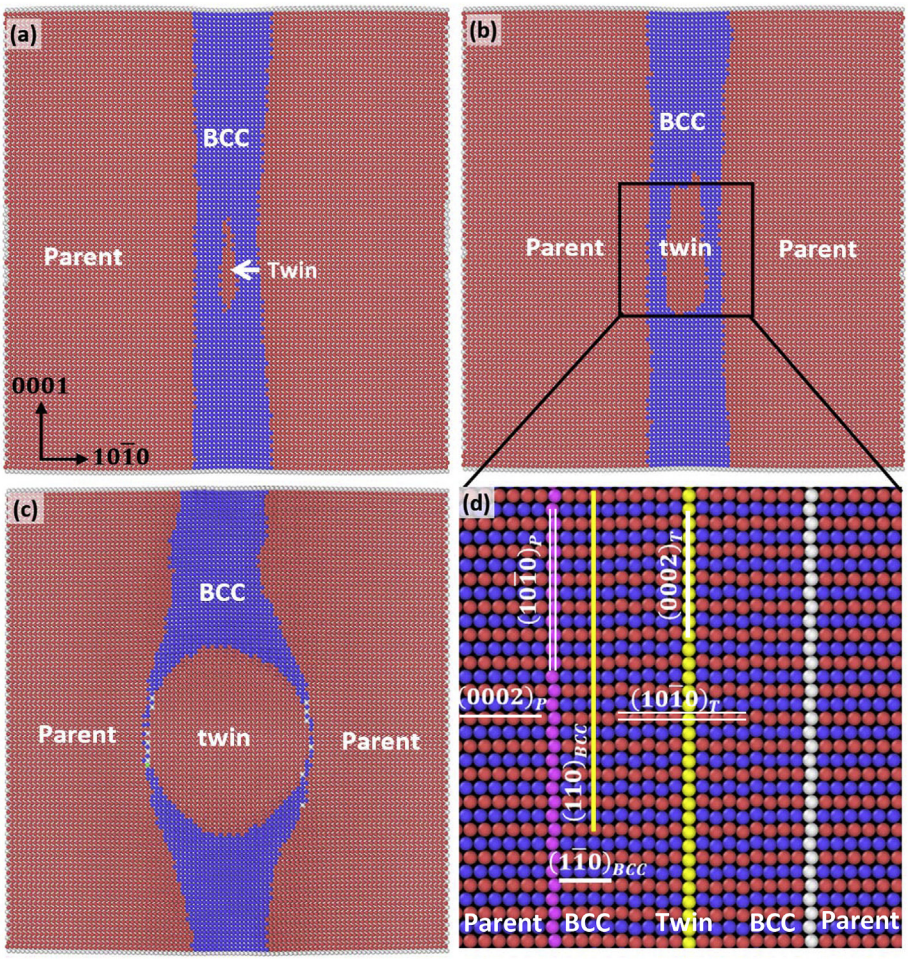

Fig. 3. (a)–(c) Common neighbor analysis (CNA) of transformation from BCC to HCP twin in time sequence. (a) New HCP lattice nucleates inside the BCC. (b) The HCP twin grows. (c) The HCP twin grows at the expense of the BCC. The interface between the BCC structure and the new HCP structure is highly incoherent. (d) Magnified view of the boxed region in (b) without CNA. The misorientation between the new HCP and the original HCP satisfies $90^\circ 1\bar{2}10$, which is a $\{10\bar{1}2\}$ twin. The orientation relationship between the HCP, BCC and HCP twin can be described as: $(0002)_P \parallel (1\bar{1}0)_{BCC} \parallel (10\bar{1}0)_T$ and $(10\bar{1}0)_P \parallel (110)_{BCC} \parallel (0002)_T$.

HCP twin. Thus, the orientation relationship between the HCP parent, BCC phase and HCP twin can be described as: $(0002)_P \parallel (1\bar{1}0)_{BCC} \parallel (10\bar{1}0)_T$ and $(10\bar{1}0)_P \parallel (110)_{BCC} \parallel (0002)_T$.

In Fig. 4a, the nucleation of FCC phase (shown in green in CNA) can be observed at the interface between the HCP parent and the HCP twin. The FCC phase at the TB grows into the parent and propagates toward the top and bottom free surfaces, forming four wedge-shaped FCC regions that separate the twin from the parent (Fig. 4b). Note that the four wedges naturally bridge the free surfaces of the parent and the twin, between which a misfit strain is produced by the twinning. It can be readily seen that an expansion in the vertical direction is produced after the BCC structure is totally consumed by the extension twin. As the straining continued, the FCC phase was transformed into the HCP twin through the gliding of the Shockley partial dislocations (denoted by the white circles) on consecutive $(111)_{FCC}$ planes. In contrast, no well-defined interfacial dislocations were observed at the interface between the FCC and parent. Fig. 4c shows the magnified view of the boxed region in Fig. 4b without CNA. The orientation relationship between these different structures can be determined as: $(10\bar{1}0)_P \parallel (111)_{FCC} \parallel (0002)_T$.

To further verify that the FCC phase at the TB was transformed from the HCP parent, the evolution of FCC at the lower right corner of the twinned region was tracked, as shown in Fig. 5. In Fig. 5a, no FCC structure can be observed because the FCC nucleus (Fig. 5a) is growing but has not reached surface region. As the strain increases, the FCC structure emerges at the interface between the parent and the twin. A local shear strain that appears to be a slope on the surface of the FCC phase can be seen (Fig. 5b). The FCC phase further expands toward the parent as the strain increases (Fig. 5c). The FCC phase keeps thickening until the misfit strain between the parent and the twin is fully accommodated by the local shear strain (Fig. 5d). Combined with Fig. 4c, it can be seen that the single layered, close-packed $(111)_{FCC}$ planes of FCC phase are transformed from the double layered $(10\bar{1}0)_P$ prismatic planes of the HCP parent. Thus, atomic shuffles must be involved in this transformation.

4. Analysis and discussion

4.1. The mechanism for HCP→BCC phase transformation

It is interesting that HCP, BCC and FCC structures were all observed in pure Ti in a single simulation of uniaxial compression perpendicular to the *c*-axis. This loading condition strongly favors extension twinning. But the BCC and FCC structures are only transitory and eventually transform back to HCP (Figs. 3–5). For the transformation of $HCP_{parent} \rightarrow BCC \rightarrow HCP_{twin}$, the orientation

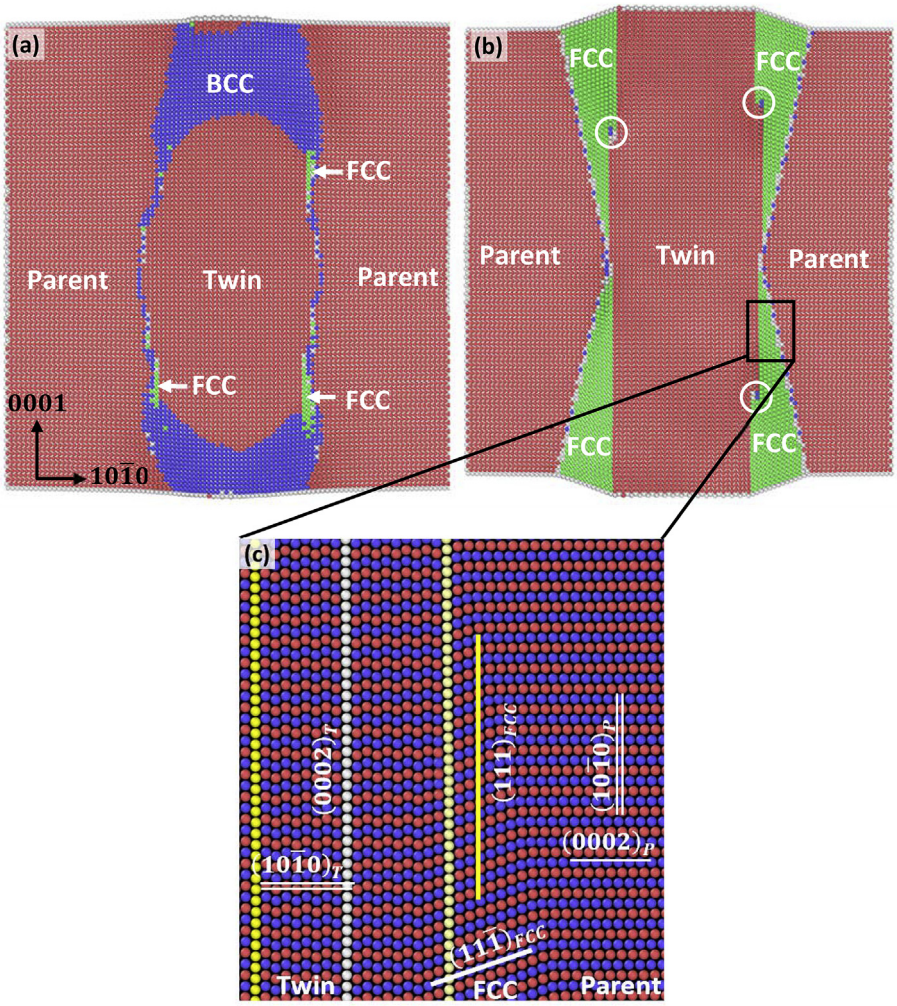

Fig. 4. (a)–(b) Common neighbor analysis (CNA) of structural evolution. (a) Nucleation of FCC phase (in green) at the twin boundary (TB). (b) The FCC phase grows by transforming the HCP parent. Meanwhile, the FCC phase transforms into the HCP twin by the glide of Shockley partial dislocations (denoted by the white circles). (c) Magnified view of the boxed region in (b) without CNA. The orientation relationship satisfies: $(10\bar{1}0)_P \parallel (111)_{FCC} \parallel (0002)_T$. (For interpretation of the references to color in this figure legend, the reader is referred to the Web version of this article.)

relationship (OR) between the phases can be described as: $(10\bar{1}0)_P \parallel (110)_{BCC} \parallel (0002)_T$ and $[1\bar{2}10]_P \parallel [001]_{BCC} \parallel [1\bar{2}10]_T$. The BCC structure disappears as the compressive strain increases. This OR is the same as the Burgers OR [42]. With this OR, six β (BCC) variants can be activated from an α (HCP) phase during the α→β phase transformation [45,46]. Conversely, twelve α variants can be generated during the β→α phase transformation [46–48]. Thus, there are 72 potential $\alpha_1 \rightarrow \beta \rightarrow \alpha_2$ phase transformation paths, including 12 paths which can restore the original α_1 orientation [46,49,50]. In terms of crystallography, the observed orientation relationship ($90^\circ\langle 1\bar{2}10\rangle$ reorientation) in this work, i.e., $\{0001\}_{\alpha_1} \parallel \{110\}_\beta \parallel \{10\bar{1}0\}_{\alpha_2}$, indeed belongs to a type of $\alpha_1 \rightarrow \beta \rightarrow \alpha_2$ phase transformation. In Appendix, it is demonstrated that when two α crystals form an OR of $90^\circ\langle 1\bar{2}10\rangle$, they are $\{10\bar{1}2\}$ twins despite the theoretical misorientation equals 85°.

The analysis of transformation mechanism from HCP parent to BCC is displayed in Fig. 6. To better understand the transformation process, the HCP (in red) lattice and the BCC (in blue) lattice obtained in the simulation were taken out and superimposed such that they have exactly the same OR as in Figs. 3 and 4. In Fig. 6a, the $(1\bar{1}0)_{BCC}$ plane of the BCC phase is superimposed on the $(0002)_P$ basal plane of the HCP parent. The viewing direction is along the [0001] of the parent. It can be seen that the projected 2D structures of the parent basal and the $(1\bar{1}0)_{BCC}$ of the BCC phase are so close that only small atomic shuffles are needed to transform a $(0002)_P$ to a $(1\bar{1}0)_{BCC}$. The atomic shuffles are denoted by the yellow arrows. As a result of the shuffling, the double-layered $(10\bar{1}0)_P$ prismatic planes of the parent become single-layered $(110)_{BCC}$ planes of the BCC. If the superimposed view is plotted along the $[10\bar{1}0]_P$ of the parent, as shown in Fig. 6b, the projected structure of the $(10\bar{1}0)_P$ parent prismatic plane is almost identical to the structure of the $(110)_{BCC}$ of the BCC phase. Minor shuffles are required such that a slight elongation in the $[1\bar{2}10]_P$ direction and a slight contraction in the $[0002]_P$ direction are produced. As such, the shuffles are able to transform the HCP parent to the BCC structure without involving any dislocation-mediated shear deformation.

The lattice transformation in Fig. 6 can be described as: $(0002)_P \rightarrow (1\bar{1}0)_{BCC}$, and $(10\bar{1}0)_P \rightarrow (110)_{BCC}$. To better reveal the transformation process, the 2D views in Fig. 6 were translated into a 3D representation of lattice transformation in Fig. 7. The HCP parent is shown as the red lattice, while the BCC unit cell is shown in blue. The atoms in red and blue are shared by both lattices. It can be observed that the shaded $(1\bar{1}0)_{BCC}$ plane and $(110)_{BCC}$ plane are

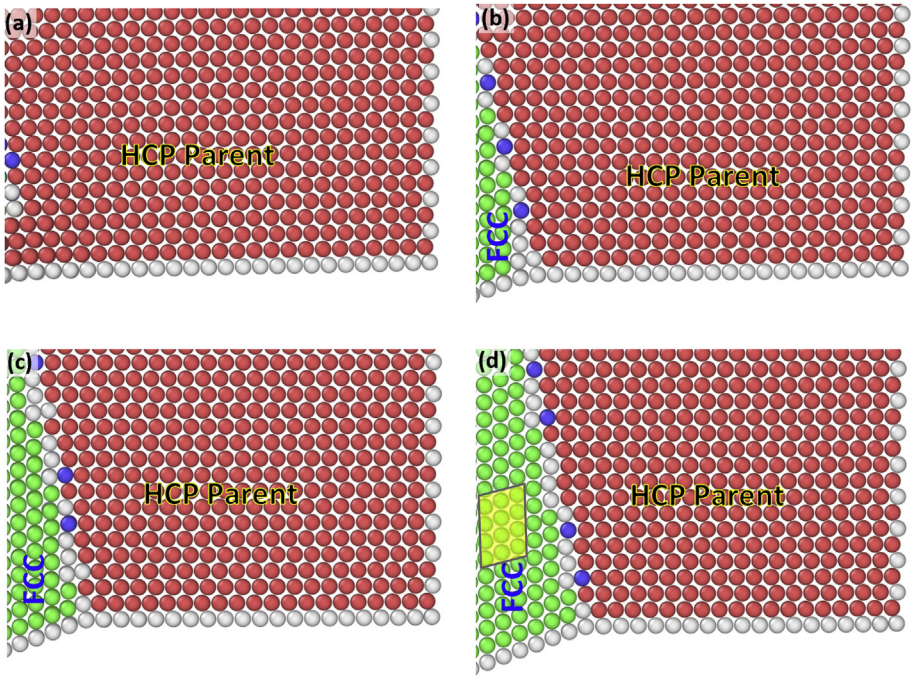

Fig. 5. The formation and growth of the FCC structure at the expense of the HCP parent lattice in time sequence. The boxed region in (d) is selected to compute the energy evolution during transformation.

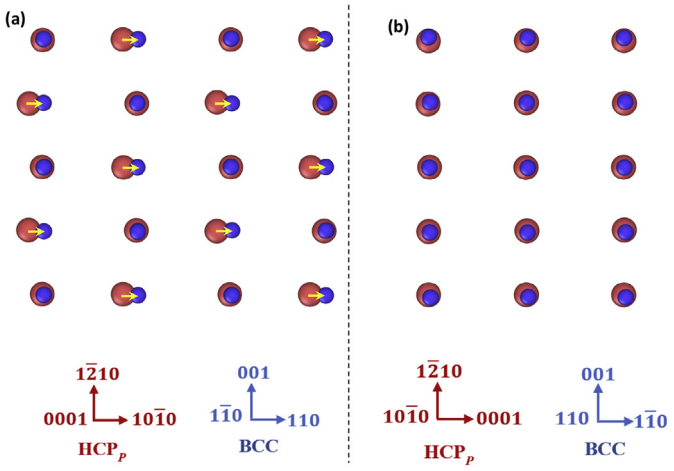

Fig. 6. Analysis of transformation from HCP parent (in red) to the BCC structure (in blue). The HCP parent and the BCC are taken from the snapshot at 106 ps and 114 ps, respectively. (a) The $(1\bar{1}0)_{BCC}$ plane of the BCC structure is superimposed on the $(0002)_P$ basal plane of the HCP parent. The major atomic shuffles are denoted by the yellow arrows which transforms the $(0002)_P$ of the HCP parent to the $(110)_{BCC}$ of the BCC. (b) The $(110)_{BCC}$ plane is superimposed on the $(10\bar{1}0)_P$ plane of HCP parent. Minor atomic shuffles are required along the [0001] and $[1\bar{2}10]$ direction. The lattice transformation can be described as: $(0002)_P \rightarrow (1\bar{1}0)_{BCC}$, and $(10\bar{1}0)_P \rightarrow (110)_{BCC}$. (For interpretation of the references to color in this figure legend, the reader is referred to the Web version of this article.)

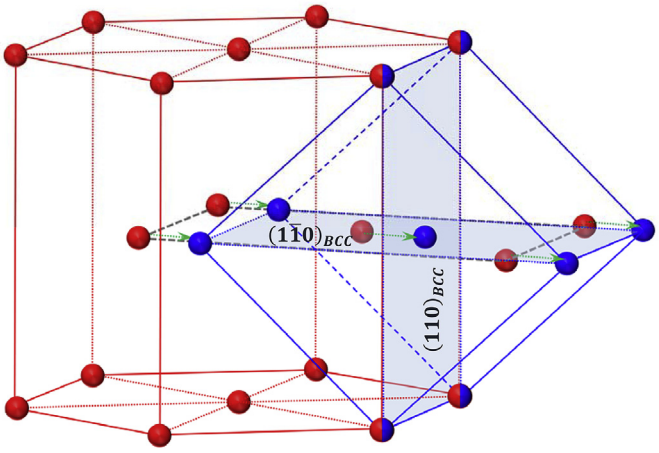

Fig. 7. 3D representation of the lattice transformation shown in Fig. 6. The HCP parent is shown in red lattice and the BCC in blue. The shaded $(1\bar{1}0)_{BCC}$ plane and $(110)_{BCC}$ plane are parallel to the basal plane and prismatic plane of the parent, respectively. The atomic shuffles (indicated by the green arrows) transform the basal and the prismatic of the parent into the two close-packed $\{110\}_{BCC}$ of the BCC. This process only involves atomic shuffles. (For interpretation of the references to color in this figure legend, the reader is referred to the Web version of this article.)

parallel to the basal plane and prismatic plane of the parent, respectively. The atomic shuffles are indicated by the green arrows. To transform the double layered $(10\bar{1}0)_P$ parent prismatic plane to the single layered $(110)_{BCC}$ plane, the atoms on every other parent basal plane must shuffle to reach the center positions of the prismatic planes, i.e. those positions indicated by the blue atoms. This lattice transformation is exactly the same as in Fig. 6. The magnitude of the atomic shuffles equals ~ $\frac{\sqrt{3}a}{6} = 0.085\ nm$, with a being the lattice parameter of HCP Ti. The major shuffles are along the $[10\bar{1}0]$ and minor shuffles are also needed along the [0001] and $[11\bar{2}0]$ such that the perfect BCC structure can be obtained. According to Ojha and Sehitoglu [43], the HCP lattice undergoes a dilation in the $[1\bar{2}10]$ and a contraction in the $[10\bar{1}0]$ when the perfect HCP lattice transforms to the perfect BCC lattice, such that the angle between the two diagonals of $(0002)_P$ plane is adjusted from 120° to 109.47° which is the angle between the two diagonals of the $(110)_{BCC}$. In fact, a contraction in the $[0002]_P$ direction is also generated and this can be seen from the slight contractions on the top and bottom surfaces (Fig. 2c). This indicates that this

transformation is dominated solely by atomic shuffling. The geometrical relationship of $(0002)_P \parallel (1\bar{1}0)_{BCC}$ and $(10\bar{1}0)_P \parallel (110)_{BCC}$ also indicates that no dislocation-mediated shear is involved, otherwise these two parallelisms would be destroyed by such shear deformation. The above analysis of the transformation process is consistent with the proposed mechanism by Li. et al. [51] in a Ti–Nb alloy via examining the atomic projections. They show that intermediate steps are involved during the transformation of the double-layered $(10\bar{1}0)_P$ plane to the single-layered $(110)_{BCC}$ close-packed plane, which only involves atomic shuffling. In the simulation results of this work, such intermediate steps seem unnecessary because the shuffles are very simple. Campbell et al. [52] observed rapid martensitic transformation from HCP to BCC, which is induced by nanosecond laser irradiation using a novel nanosecond electron microscope. Their results suggested that this transformation is driven by lattice distortion due to rapid concentration in strain energy.

As the straining continues (Fig. 3), the BCC phase transforms to HCP twin which has a misorientation of $90°\left\langle 1\bar{2}10\right\rangle$ with the HCP parent. It can be seen from Fig. 7, this transformation can be easily accomplished when the $(110)_{BCC}$ transforms to the (0002) of HCP, and the $(1\bar{1}0)_{BCC}$ transforms to the $(10\bar{1}0)$ of HCP. The lattice transformation is shown in Fig. 8. The $(0002)_T$ basal plane of the HCP twin (in red) is projected to the $(110)_{BCC}$ plane of the BCC phase (Fig. 8a). The viewing direction is along the [110]/[0001] direction. The yellow arrows represent the major atomic shuffles. From the projection view, it can be observed that the atomic shuffles on the $(110)_{BCC}$ plane along the $[1\bar{1}0]$ direction transform the $(110)_{BCC}$ to the $(0002)_T$ basal plane of the twin. Concurrently, the $(1\bar{1}0)_{BCC}$ plane is transformed to the double-layered $(10\bar{1}0)_T$ plane of twin lattice, as shown in Fig. 8b which is a projection view along the $[1\bar{1}0]/[10\bar{1}0]$ direction such that the $(10\bar{1}0)_T$ prismatic plane of the HCP twin is superimposed on the $(1\bar{1}0)_{BCC}$ plane of the BCC phase. Again, minor shuffles in the other two directions are required for the atoms to reach the perfect HCP positions. This type of transformation path, i.e., β Ti → α Ti, has been reported by a number researchers [42–44,53–56]. Burgers [42] proposed that this transformation can be accomplished by two independent processes: (1) atomic shuffling on every other $(110)_{BCC}$ plane in the $[1\bar{1}0]$ direction; (2) a shear on the $\{112\}_{BCC}$ plane along the $[11\bar{1}]_{BCC}$ direction. The results in this work show that atomic shuffles are all needed to accomplish the lattice transformation and no dislocation-mediated shear is involved.

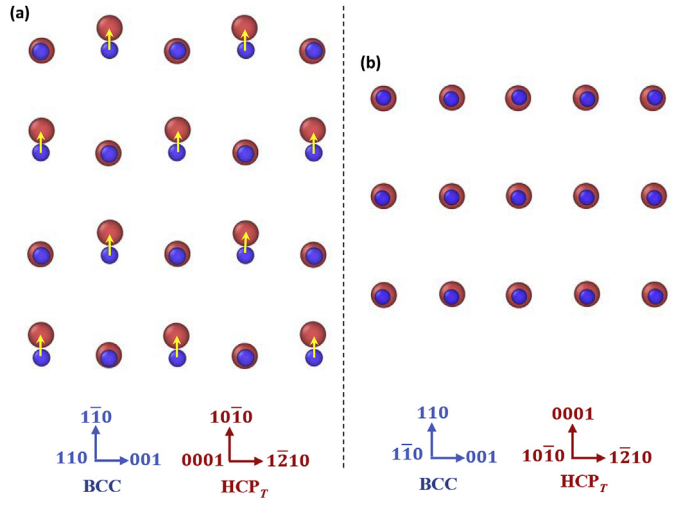

Fig. 8. The transformation from the BCC structure (in blue) to the HCP twin (in red). The BCC is taken from the snapshot at 114.5 ps, and the HCP twin is taken from the snapshot at 119 ps. (a) The $(110)_{BCC}$ of the BCC is transformed to the basal plane of the HCP twin by atomic shuffles along $[1\bar{1}0]$ direction. (b) The $(1\bar{1}0)_{BCC}$ of the BCC is transformed to the $(10\bar{1}0)_T$ of twin. Minor shuffle is observed in the [001] direction. The orientation of the new HCP is reoriented by 90° around the $1\bar{2}10$, which satisfies twin relationship with respect to the original HCP lattice. (For interpretation of the references to color in this figure legend, the reader is referred to the Web version of this article.)

4.2. The mechanism for HCP↔FCC transformation

The HCP↔FCC transformation was investigated by a number of researchers in the literature. Two types of OR between FCC and HCP were reported: (I) $\{0002\}_P \parallel \{111\}_{FCC}$ and $[11\bar{2}0]_P \parallel [110]_{FCC}$ [57–59]; (II) $\{10\bar{1}0\}_P \parallel \{1\bar{1}0\}_{FCC}$ and $[0001]_P \parallel [001]_{FCC}$[28,60–62]. For the type I OR, Zhao et al. [58] reported that the successive gliding of $\frac{1}{3}\left\langle 10\bar{1}0\right\rangle$ Shockley partials on every other basal plane is responsible for the transformation of an HCP lattice to an FCC lattice during cold rolling. These Shockley partials originate from the dissociation of full $a = \frac{1}{3}\left\langle 1\bar{2}10\right\rangle$ dislocations. Yu et al. [57] also observed an FCC phase in pure Ti by in-situ TEM, where the FCC and HCP phase have type I OR, and the transformation mechanism is also identical to that in Ref. [58]. For type II OR, the transformation mechanism is controversial. Hong et al. [60] observed a stress induced transformation of HCP to FCC under a cryogenic channel die compression. Ren et al. [28] also investigated this type of transformation by MD simulation. In both studies, they reported that $\left\{10\bar{1}0\right\}\frac{1}{6}\left\langle 11\bar{2}0\right\rangle$ Shockley partials accounted for the phase transformation. In contrast, Wu et al. [63] suggested that type II transformation can be accomplished by either a pure shuffle mechanism or a shear-shuffle mechanism. Recently, Yang et al. [64] proposed a more detailed mechanism in which the gliding of

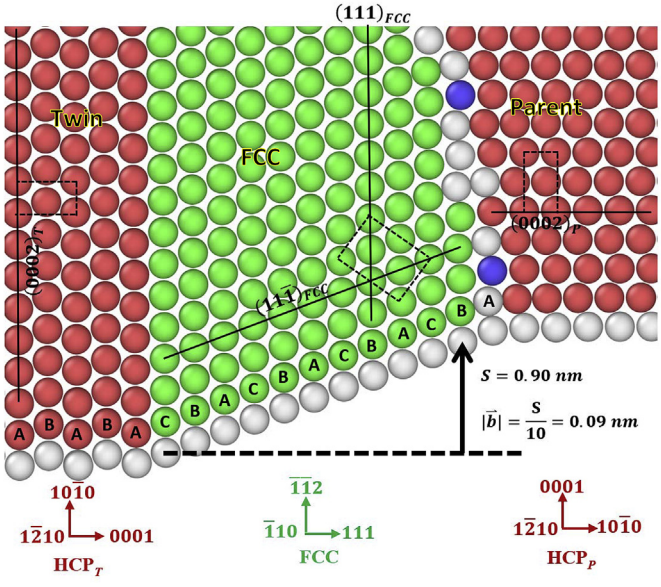

Fig. 9. Transformation of HCP parent to the FCC which separates $\{10\bar{1}2\}$ twin from the parent. A shear strain is generated to compensate the misfit strain between the parent and the twin. The displacement S over ten layers of close-packed planes is ~0.9 nm, which corresponds to a shear with half a Shockley partial dislocation on each of the ten planes. The $(111)_{FCC}$ of the FCC structure is transformed from the $(10\bar{1}0)_P$ of the parent. Meanwhile, the $(0002)_P$ basal is transformed to the $(11\bar{1})_{FCC}$. Shear and shuffles are needed for this transformation.

$\left\{10\bar{1}0\right\}\frac{1}{6}\left\langle 11\bar{2}0\right\rangle$ Shockley partials were involved, and adjustments for interplanar spacing and volume expansion were needed. In these studies, an FCC phase was embedded within and surrounded by an HCP matrix.

The OR between the FCC and HCP phase in this work is special in the sense that the FCC structure is sandwiched by the HCP parent and HCP twin. As shown in Fig. 9 which is a magnified view of Fig. 5d, the misorientation between the FCC and the HCP twin is exactly type I OR. However, the OR between the FCC and the HCP parent is a new relationship, i.e. $(10\bar{1}0)_P \parallel (111)_{FCC}$ and $[1\bar{2}10]_P \parallel [110]_{FCC}$. The overall relationship between the HCP parent, FCC and HCP twin satisfies: $(10\bar{1}0)_P \parallel (111)_{FCC} \parallel (0002)_T$. In Fig. 9, the FCC phase bridges the HCP parent and the HCP twin, and a shear can be clearly observed on the surface of the FCC. Thus, the slope on the surface serves as a strain accommodation at the TB (see more details below). The overall shear displacement $\boldsymbol{S}$ spanning over 10 layers of $(10\bar{1}0)_P$ prismatic plane is ~0.90 nm. Thus, the magnitude of the Burgers vector ($\left|\vec{b}\right|$) on each layer is ~0.090 nm, and this value corresponds to half a Shockley partial dislocation. The double layered $(10\bar{1}0)_P$ planes of the parent are transformed to the $(111)_{FCC}$ planes of the FCC. Concurrently, the $(0002)_P$ planes of the parent are transformed to the $(11\bar{1})_{FCC}$ planes of the FCC. However, the double layered $(10\bar{1}0)_P$ prismatic planes cannot transform to the single layered $(111)_{FCC}$ planes of the FCC solely by shear, so atomic shuffles have to be involved.

The detailed process of shear and shuffle involved in the $HCP_{parent} \rightarrow FCC$ transformation is schematically shown in Fig. 10. The structure of the HCP parent is plotted in Fig. 10a in which the basal planes are colored alternatively in red and blue to show the … *ABABAB* … stacking sequence. As the strain is increased sufficiently large to start TB migration, two processes occur. One of them is atomic shuffling such that a double-layered $(10\bar{1}0)_P$ right adjacent to the TB is transformed into a single-layered close-packed plane by atomic shuffling. The magnitude of the shuffle is $\sim\frac{\sqrt{3}}{6}a_{HCP}$ (Fig. 10a). These shuffles cause a dilation in the vertical direction to change the interplanar spacing of the parent basal planes from $\frac{c}{2}$ (c is the other lattice parameter of the HCP lattice) to $\frac{\sqrt{6}a_{FCC}}{4}$ (a_{FCC} is the lattice parameter of the FCC lattice). The other process involves a simple shear that occurs on each of the close-packed planes by half a Shockley partial dislocation, creating the … *ABCABC* … stacking of the FCC. Obviously, a simple shear and atomic shuffles have to occur simultaneously to accomplish the transformation. Note that, although locally the OR between the FCC and the HCP parent is $(111)_{FCC} \parallel (10\bar{1}0)_P$, the average interface is not along the $(10\bar{1}0)_P$, but close to the $(20\bar{2}1)_P$, i.e. the white and the blue atoms at the interface in Figs. 4 and 5.

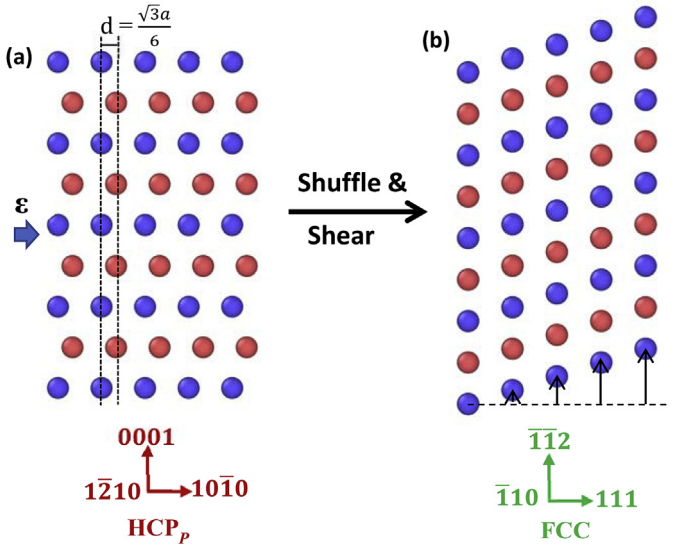

Fig. 10. Mechanism of the transformation from the HCP parent to the FCC structure. (a) The HCP parent. The basal planes are colored in red and blue to show the … *ABABAB* … stacking sequence. (b) First, a double-layered $(10\bar{1}0)_P$ is transformed into a single-layered close-packed plane by atomic shuffling. Then the close-packed plane is sheared by half a Shockley partial dislocation, creating the … *ABCABC* … stacking of the FCC. (For interpretation of the references to color in this figure legend, the reader is referred to the Web version of this article.)

For the $FCC \rightarrow HCP_{twin}$ transformation, Shockley partial dislocations are involved in this process. The partial dislocations are nucleated at the interface between the FCC and the HCP twin, and glide toward the free surfaces, as shown in Fig. 4. An enlarged view of the partial dislocation that is recovering the FCC stacking back to the HCP stacking is shown in Fig. 11a. One Shockley partial with a Burgers vector of $\frac{1}{6}[\bar{1}\bar{1}2]$ recovers two layers of the $(111)_{FCC}$ planes of the FCC to HCP stacking. In Fig. 11b, the $(0002)_T$ basal planes of the HCP twin are superimposed on the $(111)_{FCC}$ planes of the FCC. A full dislocation on the $(111)_{FCC}$ plane can dissociate into two partial dislocations:

$$\frac{1}{2}\left[\bar{1}10\right] = \frac{1}{6}\left[\bar{1}2\bar{1}\right] + \frac{1}{6}\left[\bar{2}11\right] \quad (1)$$

The gliding of a Shockley partial along the $[\bar{1}2\bar{1}]$ direction carries

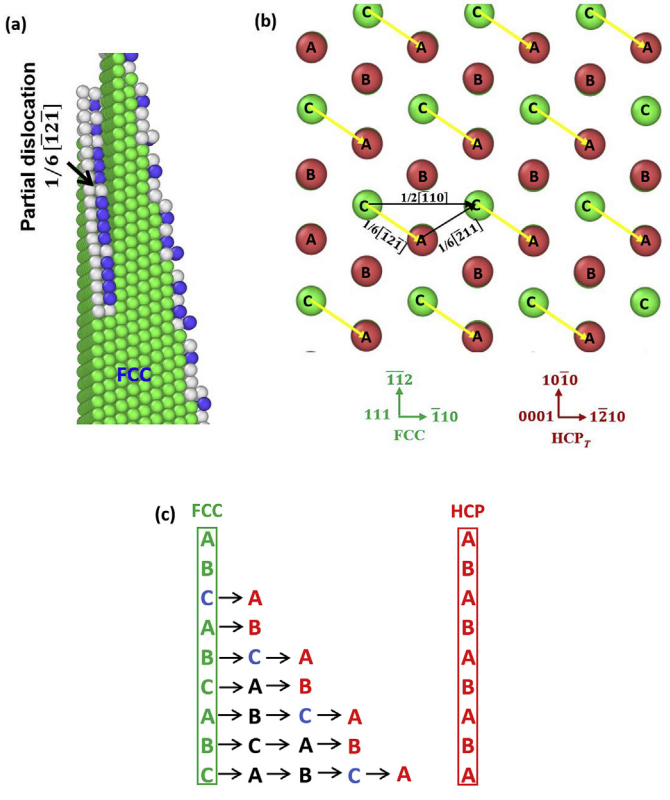

Fig. 11. Analysis of transformation from FCC to HCP twin. (a) 3D view of the Shockley partial on the $(111)_{FCC}$. (b) The $(0002)_T$ of the HCP twin is superimposed on the $(111)_{FCC}$ of the FCC. The glide of the Shockley partial carries the atoms in "C" layer to "A" layer. (c) The … ABCABC … stacking sequence of FCC structure is changed to the … ABABAB … stacking sequence of the HCP twin by Shockley partial dislocations on the interfacial $(111)_{FCC}$. Because one Shockley partial transforms two $(111)_{FCC}$ layers, partial dislocations on every other $(111)_{FCC}$ plane are only needed to transform the whole FCC phase to the HCP twin.

the atoms in the "C" layer to the "A" layer. Consequently, as shown in Fig. 11c, the … *ABCABC* … stacking sequence of the FCC is changed to the … *ABABAB* … stacking sequence of the HCP twin. Because one Shockley partial recovers two $(111)_{FCC}$ planes to the HCP stacking, Shockley partials on every other $(111)_{FCC}$ plane are needed. For example, there are ten layers of $(111)_{FCC}$ planes in the FCC in Fig. 9, only five Shockley partials are needed to completely transform the FCC to the HCP twin. This can be clearly seen in Fig. 11c in which letter notation was used to demonstrate how Shockley partials on every other $(111)_{FCC}$ planes accomplish the $FCC \rightarrow HCP_{twin}$ transformation.

4.3. Strain accommodation of the phase transformations during deformation

For deformation induced phase transformations, the volumetric strains generated in the structural transformation are effective to accommodate the plastic strain, in addition to dislocation slip and shear-induced deformation twinning. To quantitatively evaluate how much strain was accommodated by the phase transformations, the evolution of radial distribution function (RDF) of different phases that were present during deformation was plotted as shown in Fig. 12a–d. An RDF represents the probability of finding the neighbors of an atom within a certain interatomic spacing. The

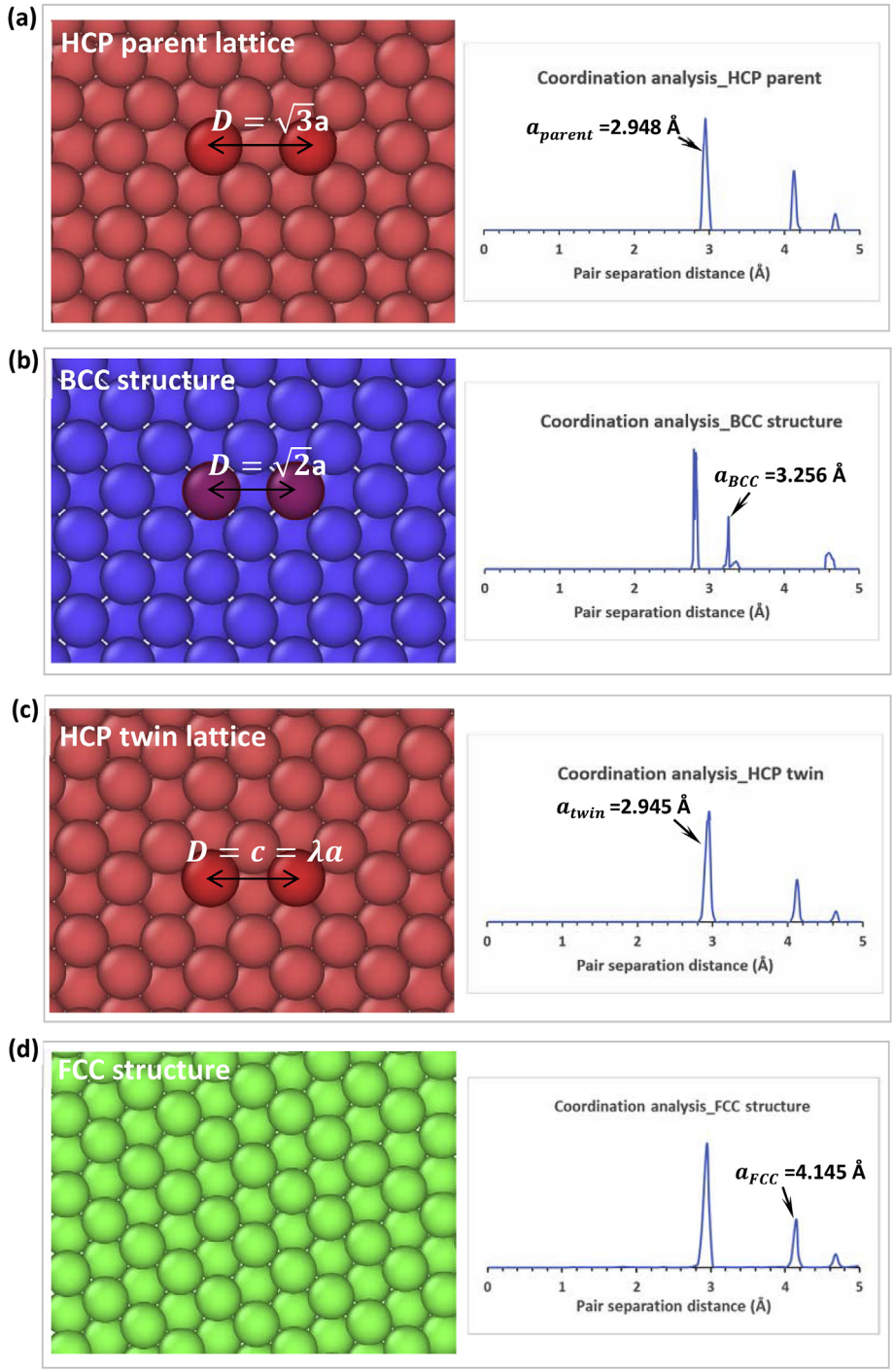

Fig. 12. The radial distribution function (RDF) of structural evolution during deformation. The characteristic peaks, which stand for the distances between nearest neighbors, represent the corresponding specific crystal structure.

characteristic peaks, which stand for the distances between nearest neighbors, correspond to a specific crystal structure. Both the parent and twin have HCP crystal structure, so the RDFs are almost identical. The lattice parameters of the parent and the twin are determined as 2.948 Å (Figs. 12a) and 2.945 Å (Fig. 12c), respectively. The minor difference in lattice parameters between the parent and the twin is due to the residual stress. Fig. 12b shows the lattice parameter of the BCC structure is 3.256 Å. A split of the peaks can be observed in Fig. 12b, indicating that the BCC structure is distorted. In Fig. 12d, the lattice parameter of the FCC structure is determined as 4.145 Å. Two atoms (highlighted in red) in a unit cell were also tracked during transformation, and the misfit strain along the loading direction can be calculated from the change of the distance between the two atoms. The misfit strain can be expressed as: $\varepsilon = \frac{D_1 - D_0}{D_0}$, where D_0 is the distance between the two tracked atoms before transformation and D_1 is the distance after transformation. Thus, the misfit strain along the loading direction for the transformation of $HCP_{parent} \rightarrow BCC$ equals $\varepsilon_1 = \frac{\sqrt{2}a_{BCC} - \sqrt{3}a_{parent}}{\sqrt{3}a_{parent}} = -9.83\%$. The misfit strain for the transformation of $BCC \rightarrow HCP_{twin}$ equals $\varepsilon_2 = \frac{\lambda a_{twin} - \sqrt{2}a_{BCC}}{\sqrt{2}a_{BCC}} = 1.58\%$ ($\lambda = \frac{c}{a} = 1.588$ for HCP Ti). The net misfit strain along the loading direction generated by $\{10\bar{1}2\}$ twinning equals $\varepsilon_{total} = \frac{\lambda a_{twin} - \sqrt{3}a_{parent}}{\sqrt{3}a_{parent}} = -8.3\%$, and no shear strain was produced by twinning.

The presence of the FCC phase at the $\{10\bar{1}2\}$ TB is also a manifestation of strain accommodation. As shown in Fig. 13a, in addition to the strain component along the loading direction, another strain component perpendicular to the loading direction is also generated, and this component equals $\frac{\sqrt{3}a_{twin} - \lambda a_{parent}}{\lambda a_{parent}} = 9.1\%$. This strain creates a dilation along the *c*-axis of the parent. Thus, the continuity of the material requires that the parent lattice near the junction of the TB and the free surfaces experience a tensile strain, whereas the twin lattice near the junction of the TB and the free surfaces experience a compressive strain (Fig. 13a). This strain localization produces the driving force for the $HCP_{parent} \rightarrow FCC$ phase transformation. As a result, the FCC phase is nucleated and forms the wedge-shaped regions right on the TB (Fig. 13b).

The transitory phase transformations, i.e. the presence of BCC and FCC phases as intermediate structures during $\left\{10\bar{1}2\right\}\left\langle 10\bar{1}\bar{1}\right\rangle$ twinning strongly suggests that this most common twinning mode in HCP metals cannot be mediated by "twinning dislocations" and no twinning shear on the $\{10\bar{1}2\}$ twinning plane should be involved [17–21,65,66].

4.4. Energetics of the phase transformations during deformation

To gain a deeper insight into how the transitory phase transformations occur during deformation twinning, it is necessary to quantitatively evaluate the energies of different crystal structures of pure Ti and the energy barriers for the lattice transformations. A question that needs to be answered is whether the phase transformations are triggered by the strain energy or by the difference in lattice energy of these phases. To this end, the equilibrium lattice energy of these three structures were calculated. The calculation with the EAM potential [32] potential for Ti is shown Fig. 14a. It can be seen that the HCP has the lowest energy (−4.85 eV/atom) at the equilibrium lattice parameter (0.295 nm). This energy is 30 meV/atom lower than that of the BCC, and 10 meV/atom lower than that of the FCC. The calculated energies are consistent with the values reported by Zope and Mishin [32] who showed that the energy of the FCC and the BCC is 11 meV/atom and 30 meV/atom higher than that of the HCP.

For comparison to the atomistic calculations, DFT calculations of

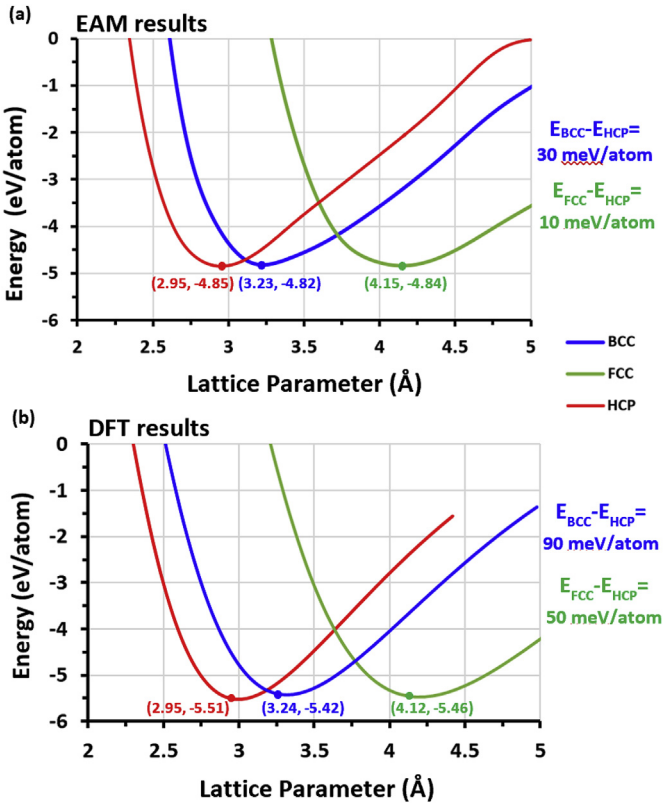

Fig. 14. (a) Energy-lattice parameter relations for different crystalline structures of Ti calculated with the EAM potential. (b) Energy-lattice parameter relations for different crystalline structures of Ti calculated with VASP.

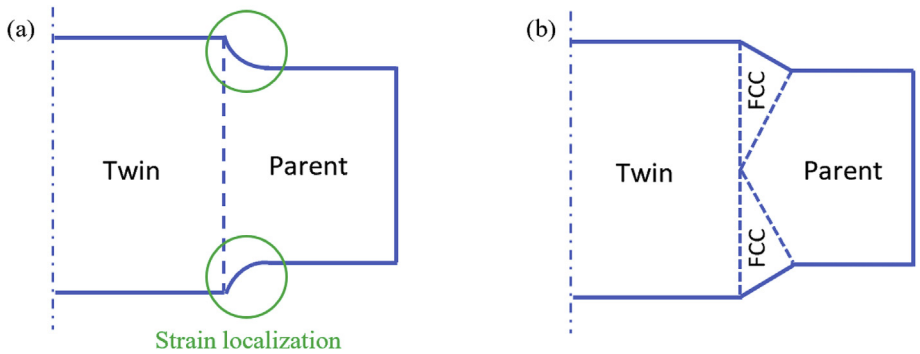

Fig. 13. Strain accommodation by the presence of the FCC phase at the TB. (a) Without the FCC, strain localization occurs because of the misfit strain between the parent and the twin lattices. (b) The strain localization is mitigated by the formation of the FCC phase at the TB.

Table 1
Comparison of the cohesive energy (eV/atom) of HCP Ti.

Present work (EAM)	Present work (DFT)	Experiment [68]	Zope and Mishin [32] (EAM)	Hennig et al. [71] (DFT)	Kim et al. [69] (MEAM)	Mehl et al. [67] (DFT)	Baskes et al. [70] (MEAM)	Gibson et al. [72] (DFT)
4.85	5.51	4.85	4.85	5.17	4.87	4.86	4.87	5.55

the lattice energies of the three crystal structures of Ti were also performed, and the results are shown in Fig. 14b. Compared to the results from the EAM potential (Fig. 14a), the DFT calculations generate similar energy differences. It is seen that the HCP Ti has the lowest energy and the BCC has the highest energy. The ground state HCP structure is 90 meV/atom and 50 meV/atom lower in energy than the BCC and the FCC structures, despite that these values are three to five times larger than the results obtained from the EAM potential. Using DFT, Mehl et al. [67] reported that the energy difference between the HCP and the FCC is 13 meV/atom, and the energy difference between the HCP and the BCC is 67 meV/atom. These atomistic calculations and DFT calculations indicate that the transitory phase transformations were triggered by the external strain in the simulations.

Table 1 summarizes the calculation results in this work and some of the values in the literature [67–72]. It can be found that our results are in good agreement with the experimental and the simulation results reported by other researchers. It should be noted that the energies from our DFT calculations are lower than those from the semi-empirical EAM and MEAM potentials. This issue is well known when DFT is applied for the transition metals [73]. Overall, the EAM potential gives a good description of the equilibrium lattice energy of different crystal structures. The calculations using the EAM and the DFT indicate that the energy differences between the BCC and the HCP, the FCC and the HCP are not high, especially for the two close-packed structures, the energies are pretty close. Thus, the transitory phase transformations in this work occurred as a result of strain accommodation.

The atomistic simulations also allow one to calculate the energy barriers for the transitory phase transformations. To perform these calculations, groups of atoms were selected and the evolution of the average energy of these atoms during deformation were calculated and plotted. The locations of selected atoms are shown in Figs. 2b and 5d. The result for the $HCP_{parent} \rightarrow BCC$ transformations is shown in Fig. 15. The boxed region in Fig. 2b contains 154 atoms. The evolution of the crystal structure of the selected atoms during deformation is also superimposed on the figure. As the deformation proceeds, the energy gradually increases as a result of the elastic strain. As the external strain further increases, at ~110 ps, a sharp increase in the energy can be seen, which corresponds to the initiation of the $HCP_{parent} \rightarrow BCC$ transformation. A careful examination reveals a small plateau before the peak energy, which comes from the growth of the BCC phase. At ~115 ps, the energy reaches a maximum followed by a plummet which signals the beginning of the $BCC \rightarrow HCP_{twin}$ transformation. The energy peak (−4.81 eV/atom) is slightly higher than the equilibrium value (−4.82 eV/atom, Fig. 14a) due to the strain energy. The energy barrier of the dynamic $HCP_{parent} \rightarrow BCC$ transformation is ~38 meV/atom. Compared to the energy difference of the ground state in Fig. 14a (30 meV/atom), this value is reasonable.

The energy barrier for the $HCP_{parent} \rightarrow FCC$ transformation is also shown in Fig. 15. 136 atoms are contained in the boxed region of Fig. 5d. The evolution of the crystal structure of the selected atoms is also superimposed on the figure. After the external strain is applied, the energy increases as the deformation proceeds. At ~110 ps, an energy drop occurs which corresponds to the energy drop caused by the $BCC \rightarrow HCP_{twin}$ transformation. Then a sharp increase

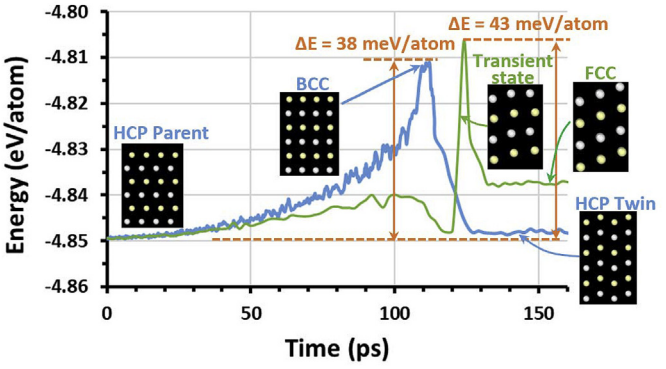

Fig. 15. Energy evolution of the selected region during transformation from HCP to BCC (in blue) and from HCP to FCC (in green). The energy barriers are ~38 meV/atom and ~43 meV/atom, respectively. (For interpretation of the references to color in this figure legend, the reader is referred to the Web version of this article.)

in energy occurs at 120 ps, corresponding to the beginning of the $HCP_{parent} \rightarrow FCC$ transformation. As indicated in the snapshot, the left layer of the double-layered prismatic plane of the HCP parent is becoming a single-layered close-packed plane of FCC. As the deformation further proceeds, the energy plummets and the transformation to the FCC is completed. The energy barrier of the dynamic $HCP_{parent} \rightarrow FCC$ transformation is ~43 meV/atom, which is slightly higher than that for the $HCP_{parent} \rightarrow BCC$ transformation. The higher energy barrier is likely due to the fact that the pathway for this $HCP_{parent} \rightarrow FCC$ transformation is more complex and both shear and shuffle are involved.

5. Conclusions

Atomistic simulations of $\{10\bar{1}2\}\langle 10\bar{1}\bar{1}\rangle$ twinning in pure Ti was conducted by applying a compressive strain perpendicular to the *c*-axis of a single crystal. Transitory phase transformations were observed during deformation. Lattice correspondence analyses were performed to resolve the mechanisms for these phase transformations. The following conclusions can be reached:

1. A transitory BCC phase was observed prior to $\{10\bar{1}2\}$ twin nucleation. Then a $\{10\bar{1}2\}$ twin nucleated inside the BCC phase. The OR between the HCP parent, the BCC phase and the HCP twin can be described as: $(10\bar{1}0)_P \parallel (110)_{BCC} \parallel (0002)_T$ and $[1\bar{2}10]_P \parallel [001]_{BCC} \parallel [1\bar{2}10]_T$. The transformation from HCP parent to the BCC phase is dominated by atomic shuffling. The transformation process can be described as: $(10\bar{1}0)_P \rightarrow (110)_{BCC}$, and $(0002)_P \rightarrow (1\bar{1}0)_{BCC}$. The transformation process from the BCC to the HCP twin can be described as: $(110)_{BCC} \rightarrow (0002)_{Twin}$, and $(1\bar{1}0)_{BCC} \rightarrow (10\bar{1}0)_{Twin}$. This process is also dominated by atomic shuffling.
2. A transitory FCC phase was also formed at the TB. The OR among the HCP parent, the FCC and the HCP twin can be described as: $(10\bar{1}0)_P \parallel (111)_{FCC} \parallel (0002)_T$. The FCC phase was formed due to the misfit strain between the parent and the twin. During twinning, a dilation perpendicular to the loading direction

occurs, causing localized strains at the junction between the TB and the free surfaces. The formation of the FCC phase at the TB mitigates the strain localization. The $HCP_{parent} \rightarrow FCC$ transformation is accomplished by both shear and atomic shuffles. Shuffling transforms the double layered $(10\bar{1}0)_P$ plane into a close-packed $(111)_{FCC}$ plane, and a shear with a Burgers vector of half a Shockley partial dislocation on the $(111)_{FCC}$ plane generates the correct FCC structure.

3. Energy calculations show that the HCP structure has the lowest energy among the three crystal structures. Although the BCC phase has the highest energy, the $HCP_{parent} \rightarrow BCC$ transformation can serve as an intermediate structure for the $\{10\bar{1}2\}$ twinning because the atomic shuffles required in this transformation are simple. The presence of the BCC and the FCC phases during twinning unambiguously demonstrates that no twinning dislocations should be involved in this particular twinning mode.

Acknowledgements

Bin Li gratefully thanks the support from the U.S. National Science Foundation (NSF) (CMMI-1635088).

Appendix. Lattice correspondence analysis of $\{10\bar{1}2\}\langle 10\bar{1}1\rangle$ twinning

In the framework of classical twinning theory [1], deformation twinning is accomplished by a homogeneous simple shear on the twinning plane, i.e., the first invariant plane K_1. The simple shear is achieved by twinning dislocations which can only glide on the twinning plane. As a result, the actual twin boundary (TB) should coincide with the twinning plane. This is the case except for $\{10\bar{1}2\}\langle 10\bar{1}1\rangle$ mode. Extensive experimental observations have shown that $\{10\bar{1}2\}$ TBs can be extremely incoherent and largely depart from the twinning plane [18,74] and the misorientation angle between the parent and twin does not have a unique value [25,74]. In most of the atomistic simulations, the misorientation angle between the parent and twin equals 90° rather than the theoretical values (85° for Ti and 86.3° for Mg) [9,17,26,29,75]. Two examples are shown in Figure A1.

Figure A1(a) shows the simulation result of $\{10\bar{1}2\}$ TB migration in pure Mg [75]. The misorientation angle equals 90°. Solid, red lines are added to the original figure to mark out the traces of the (0002) and $\{10\bar{1}0\}$ planes in the crystals λ and μ. From the red atoms on the top surface, it can be seen that the (0002) of λ has transformed to the $\{10\bar{1}0\}$ of μ. Reciprocally, the $\{10\bar{1}0\}$ of λ has transformed to the (0002) of μ. Because the misorientation angle equals 90°, $(0002)_\lambda \parallel \{10\bar{1}0\}_\mu$ and $\{10\bar{1}0\}_\lambda \parallel (0002)_\mu$. Thus, the magnitude of twinning shear should be zero because any non-zero twinning shear would destroy these two parallelisms. Figure A1(b) shows a similar analysis on the simulation result reported by Hirth et al. [29]. In this case, the misorientation angle between the parent and twin also equals 90°. Solid, red lines are added to the original figure to show the same lattice transformation. Thus, the magnitude of twinning shear should be zero as well.

The "parent basal to twin prismatic and parent prismatic to twin basal" lattice transformation in Figure A1 can be translated into a 3D representation shown in Figure A2 [17], which was proposed by Li and Ma [65]. The $\{10\bar{1}0\}$ of parent (red lattice) is transformed to the (0002) of twin (blue lattice), and the (0002) of parent is transformed to the $\{10\bar{1}0\}$ of twin. It can be seen that the two lattices satisfy $\{10\bar{1}2\}\langle 10\bar{1}1\rangle$ twin relationship because the shaded plane is perfectly shared by both lattices. But the twin lattice is distorted. To correct the distortion, atomic shuffles are required. The shuffles will distort the shaded twinning plane and thus the invariant plane strain condition in classical twinning is not satisfied. This is the root cause of all the anomalous properties of $\{10\bar{1}2\}\langle 10\bar{1}1\rangle$ twinning.

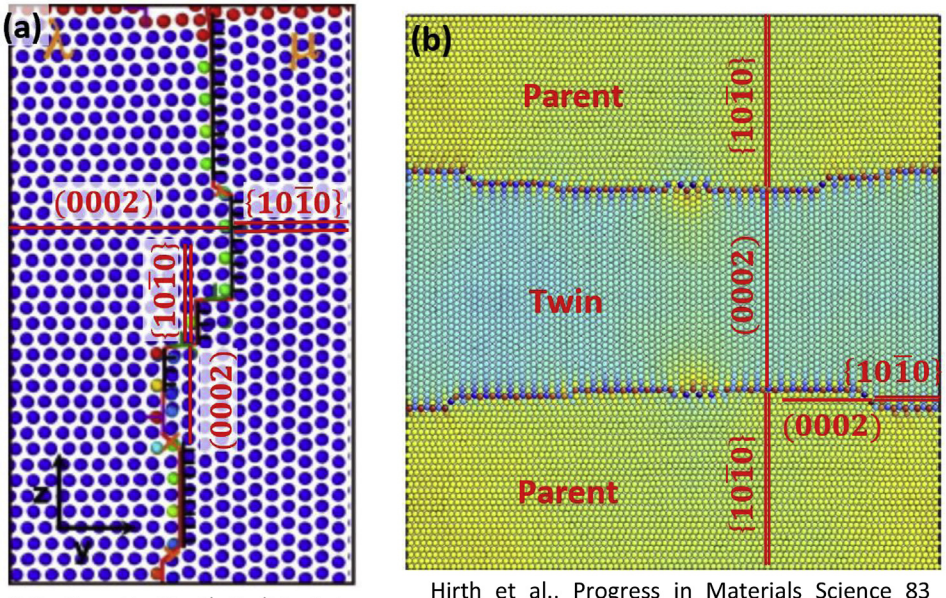

C.D. Barrett, H. El Kadiri, Acta Materialia 63 (2014) 1–15 [75].

Hirth et al., Progress in Materials Science 83 (2016) 417–471 [29].

Fig. A1. Two examples of $\{10\bar{1}2\}$ twinning in which the misorientation angle equals 90° [29,75] (with permission from Elsevier). Solid, red lines are added to the original figures to show the lattice transformation. In both cases, the lattice transformation can be recognized as "parent basal to twin prismatic and parent prismatic to twin basal" which is exactly the same as the Li-Ma shuffling model [65]. A 3D representation of the lattice transformation is shown in figure A2.

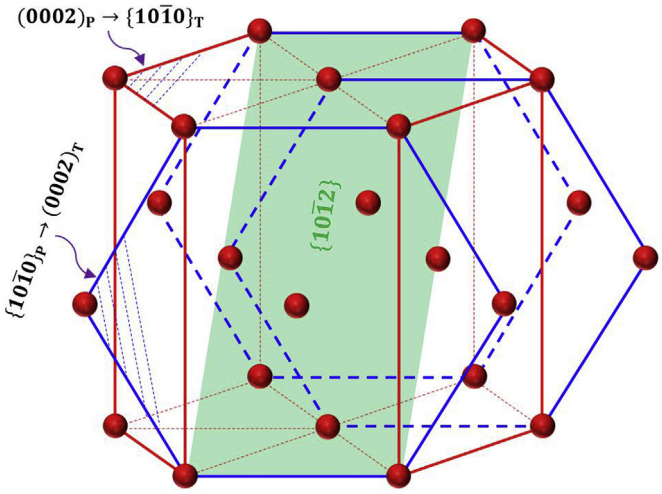

Fig. A2. 3D representation of the lattice transformation in Figure A1(a) and (b) during $\{10\bar{1}2\}$ TB migration (adapted from Ref. [17] with permission from Elsevier). This lattice transformation is exactly the same as the Li-Ma shuffling model [65] in which the parent prismatic is transformed to the twin basal and the parent basal is transformed to the twin prismatic.

References

[1] J.W. Christian, S. Mahajan, Deformation twinning, Prog. Mater. Sci. 39 (1995) 1–157.

[2] M.H. Yoo, Slip, twinning, and fracture in hexagonal close-packed metals, Metallurgical Transactions A 12 (1981) 409–418.

[3] P. Chen, B. Li, D. Culbertson, Y. Jiang, Negligible effect of twin-slip interaction on hardening in deformation of a Mg-3Al-1Zn alloy, Mater. Sci. Eng. 729 (2018) 285–293, https://doi.org/10.1016/j.msea.2018.05.067.

[4] Y. Xin, M. Wang, Z. Zeng, M. Nie, Q. Liu, Strengthening and toughening of magnesium alloy by {1 0 −1 2} extension twins, Scripta Mater. 66 (2012) 25–28, https://doi.org/10.1016/j.scriptamat.2011.09.033.

[5] J.F. Nie, Y.M. Zhu, J.Z. Liu, X.Y. Fang, Periodic segregation of solute atoms in fully coherent twin boundaries, Science 340 (2013) 957–960, https://doi.org/10.1126/science.1229369.

[6] P. Chen, B. Li, D. Culbertson, Y. Jiang, Contribution of extension twinning to plastic strain at low stress stage deformation of a Mg-3Al-1Zn alloy, Mater. Sci. Eng. 709 (2018) 40–45, https://doi.org/10.1016/j.msea.2017.10.038.

[7] D. Culbertson, Q. Yu, J. Wang, Y. Jiang, Pre-compression effect on microstructure evolution of extruded pure polycrystalline magnesium during reversed tension load, Mater. Char. 134 (2017) 41–48, https://doi.org/10.1016/j.matchar.2017.10.003.

[8] P. Chen, F. Wang, B. Li, Dislocation absorption and transmutation at {10-12} twin boundaries in deformation of magnesium, Acta Mater. 164 (2019) 440–453, https://doi.org/10.1016/j.actamat.2018.10.064.

[9] J. Wang, S.K. Yadav, J.P. Hirth, C.N. Tomé, I.J. Beyerlein, Pure-shuffle nucleation of deformation twins in hexagonal-close-packed metals, Materials Research Letters 1 (2013) 126–132, https://doi.org/10.1080/21663831.2013.792019.

[10] P. Chen, F. Wang, J. Ombogo, B. Li, Formation of 60° ⟨01-10⟩ boundaries between {10-12} twin variants in deformation of a magnesium alloy, Mater. Sci. Eng. 739 (2019) 173–185, https://doi.org/10.1016/j.msea.2018.10.029.

[11] T. Ezaz, M.D. Sangid, H. Sehitoglu, Energy barriers associated with slip–twin interactions, Phil. Mag. 91 (2011) 1464–1488, https://doi.org/10.1080/14786435.2010.541166.

[12] X. Li, Y. Wei, L. Lu, K. Lu, H. Gao, Dislocation nucleation governed softening and maximum strength in nano-twinned metals, Nature 464 (2010) 877–880, https://doi.org/10.1038/nature08929.

[13] Y.T. Zhu, X.L. Wu, X.Z. Liao, J. Narayan, L.J. Kecskés, S.N. Mathaudhu, Dislocation–twin interactions in nanocrystalline fcc metals, Acta Mater. 59 (2011) 812–821, https://doi.org/10.1016/j.actamat.2010.10.028.

[14] B. Li, E. Ma, Zonal dislocations mediating {101-1}⟨10-1-2⟩ twinning in magnesium, Acta Mater. 57 (2009) 1734–1743, https://doi.org/10.1016/j.actamat.2008.12.016.

[15] Y.M. Zhu, S.W. Xu, J.F. Nie, {10-11} Twin boundary structures in a Mg–Gd alloy, Acta Mater. 143 (2018) 1–12, https://doi.org/10.1016/j.actamat.2017.09.067.

[16] B. Li, H.E. Kadiri, M.F. Horstemeyer, Extended zonal dislocations mediating twinning in titanium, Phil. Mag. 92 (2012) 1006–1022, https://doi.org/10.1080/14786435.2011.637985.

[17] B. Li, X.Y. Zhang, Twinning with zero twinning shear, Scripta Mater. 125 (2016) 73–79, https://doi.org/10.1016/j.scriptamat.2016.07.004.

[18] X.Y. Zhang, B. Li, X.L. Wu, Y.T. Zhu, Q. Ma, Q. Liu, P.T. Wang, M.F. Horstemeyer, Twin boundaries showing very large deviations from the twinning plane, Scripta Mater. 67 (2012) 862–865, https://doi.org/10.1016/j.scriptamat.2012.08.012.

[19] C. Cayron, R. Logé, Evidence of new twinning modes in magnesium questioning the shear paradigm, J. Appl. Crystallogr. 51 (2018) 809–817, https://doi.org/10.1107/S1600576718005678.

[20] S.G. Song, G.T. Gray, Structural interpretation of the nucleation and growth of deformation twins in Zr and Ti—II. Tem study of twin morphology and defect reactions during twinning, Acta Metall. Mater. 43 (1995) 2339–2350, https://doi.org/10.1016/0956-7151(94)00434-X.

[21] S.G. Song, G.T. Gray, Structural interpretation of the nucleation and growth of deformation twins in Zr and Ti—I. Application of the coincidence site lattice (CSL) theory to twinning problems in h.c.p. structures, Acta Metall. Mater. 43 (1995) 2325–2337, https://doi.org/10.1016/0956-7151(94)00433-1.

[22] P.G. Partridge, The crystallography and deformation modes of hexagonal close-packed metals, Metall. Rev. 12 (1967) 169–194.

[23] M.A. Gharghouri, G.C. Weatherly, J.D. Embury, The interaction of twins and precipitates in a Mg-7.7 at.% Al alloy, Philos. Mag. A 78 (1998) 1137–1149, https://doi.org/10.1080/01418619808239980.

[24] B.-Y. Liu, J. Wang, B. Li, L. Lu, X.-Y. Zhang, Z.-W. Shan, J. Li, C.-L. Jia, J. Sun, E. Ma, Twinning-like lattice reorientation without a crystallographic twinning plane, Nat. Commun. 5 (2014), https://doi.org/10.1038/ncomms4297.

[25] X.Y. Zhang, B. Li, Q. Sun, On the {10-12} "twinning shear" measured from line deflection, Scripta Mater. 159 (2019) 133–136, https://doi.org/10.1016/j.scriptamat.2018.09.027.

[26] X.Y. Zhang, B. Li, Q. Liu, Non-equilibrium basal stacking faults in hexagonal close-packed metals, Acta Mater. 90 (2015) 140–150, https://doi.org/10.1016/j.actamat.2015.02.036.

[27] A. Serra, D.J. Bacon, A new model for {10-12} twin growth in hcp metals, Philos. Mag. A 73 (1996) 333–343, https://doi.org/10.1080/01418619608244386.

[28] J. Ren, Q. Sun, L. Xiao, X. Ding, J. Sun, Phase transformation behavior in titanium single-crystal nanopillars under [0001] orientation tension: a molecular dynamics simulation, Comput. Mater. Sci. 92 (2014) 8–12, https://doi.org/10.1016/j.commatsci.2014.05.018.

[29] J.P. Hirth, J. Wang, C.N. Tomé, Disconnections and other defects associated with twin interfaces, Prog. Mater. Sci. 83 (2016) 417–471, https://doi.org/10.1016/j.pmatsci.2016.07.003.

[30] M.S. Daw, M.I. Baskes, Embedded-atom method: derivation and application to impurities, surfaces, and other defects in metals, Phys. Rev. B 29 (1984) 6443–6453, https://doi.org/10.1103/PhysRevB.29.6443.

[31] M.S. Daw, M.I. Baskes, Semiempirical, quantum mechanical calculation of hydrogen embrittlement in metals, Phys. Rev. Lett. 50 (1983) 1285–1288, https://doi.org/10.1103/PhysRevLett.50.1285.

[32] R.R. Zope, Y. Mishin, Interatomic potentials for atomistic simulations of the Ti-Al system, Phys. Rev. B 68 (2003), https://doi.org/10.1103/PhysRevB.68.024102, 024102.

[33] Z.-C. Xie, T.-H. Gao, X.-T. Guo, Q. Xie, Molecular dynamics simulation of nanocrystal formation and deformation behavior of Ti3Al alloy, Comput. Mater. Sci. 98 (2015) 245–251, https://doi.org/10.1016/j.commatsci.2014.10.012.

[34] A. Stukowski, Visualization and analysis of atomistic simulation data with OVITO–the open visualization tool, Model. Simulat. Mater. Sci. Eng. 18 (2010), 015012, https://doi.org/10.1088/0965-0393/18/1/015012.

[35] J.D. Honeycutt, H.C. Andersen, Molecular dynamics study of melting and freezing of small Lennard-Jones clusters, J. Phys. Chem. 91 (1987) 4950–4963, https://doi.org/10.1021/j100303a014.

[36] G. Kresse, J. Hafner, Ab initio molecular dynamics for liquid metals, Phys. Rev. B 47 (1993) 558–561, https://doi.org/10.1103/PhysRevB.47.558.

[37] G. Kresse, J. Furthmüller, Efficiency of ab-initio total energy calculations for metals and semiconductors using a plane-wave basis set, Comput. Mater. Sci. 6 (1996) 15–50, https://doi.org/10.1016/0927-0256(96)00008-0.

[38] G. Kresse, J. Furthmüller, Efficient iterative schemes for ab initio total-energy calculations using a plane-wave basis set, Phys. Rev. B 54 (1996) 11169–11186, https://doi.org/10.1103/PhysRevB.54.11169.

[39] P.E. Blöchl, Projector augmented-wave method, Phys. Rev. B 50 (1994) 17953–17979, https://doi.org/10.1103/PhysRevB.50.17953.

[40] G. Kresse, D. Joubert, From ultrasoft pseudopotentials to the projector augmented-wave method, Phys. Rev. B 59 (1999) 1758–1775, https://doi.org/10.1103/PhysRevB.59.1758.

[41] J.P. Perdew, K. Burke, M. Ernzerhof, Generalized gradient approximation made simple, Phys. Rev. Lett. 77 (1996) 3865–3868, https://doi.org/10.1103/PhysRevLett.77.3865.

[42] W.G. Burgers, On the process of transition of the cubic-body-centered modification into the hexagonal-close-packed modification of zirconium, Physica 1 (1934) 561–586, https://doi.org/10.1016/S0031-8914(34)80244-3.

[43] A. Ojha, H. Sehitoglu, Critical stress for the bcc–hcp martensite nucleation in Ti–6.25at.%Ta and Ti–6.25at.%Nb alloys, Comput. Mater. Sci. 111 (2016) 157–162, https://doi.org/10.1016/j.commatsci.2015.08.050.

[44] P. Dang, M. Grujicic, Atomistic simulation of transformation toughening in Ti-V b.c.c. beta phase, Scripta Mater. 35 (1996) 59–64, https://doi.org/10.1016/1359-6462(96)00101-7.

[45] M.G. Glavicic, P.A. Kobryn, T.R. Bieler, S.L. Semiatin, A method to determine the orientation of the high-temperature beta phase from measured EBSD data for the low-temperature alpha phase in Ti-6Al-4V, Mater. Sci. Eng. 346 (2003) 50–59, https://doi.org/10.1016/S0921-5093(02)00535-X.

[46] L. Zeng, T.R. Bieler, Effects of working, heat treatment, and aging on microstructural evolution and crystallographic texture of α, α′, α″ and β phases in Ti–6Al–4V wire, Mater. Sci. Eng. 392 (2005) 403–414, https://doi.org/10.1016/j.msea.2004.09.072.
[47] T.R. Bieler, M.G. Glavicic, S.L. Semiatin, Using OIM to investigate the microstructural evolution of Ti-6Ai-4V, J. Occup. Med. 54 (2002) 31–36, https://doi.org/10.1007/BF02822602.
[48] T.R. Bieler, S.L. Semiatin, The origins of heterogeneous deformation during primary hot working of Ti–6Al–4V, Int. J. Plast. 18 (2002) 1165–1189, https://doi.org/10.1016/S0749-6419(01)00057-2.
[49] C. Cayron, Importance of the α→β transformation in the variant selection mechanisms of thermomechanically processed titanium alloys, Scripta Mater. 59 (2008) 570–573, https://doi.org/10.1016/j.scriptamat.2008.05.013.
[50] M.R. Daymond, R.A. Holt, S. Cai, P. Mosbrucker, S.C. Vogel, Texture inheritance and variant selection through an hcp–bcc–hcp phase transformation, Acta Mater. 58 (2010) 4053–4066, https://doi.org/10.1016/j.actamat.2010.03.012.
[51] Y. Li, J. Li, B. Liu, The atomistic mechanism of hcp-to-bcc martensitic transformation in the Ti–Nb system revealed by molecular dynamics simulations, Phys. Chem. Chem. Phys. 17 (2015) 4184–4192, https://doi.org/10.1039/C4CP04894F.
[52] G. Campbell, T. LaGrange, W. King, J. Colvin, A. Ziegler, N. Browning, H. Kleinschmidt, O. Bostanjoglo, The HCP to BCC Phase Transformation in Ti Characterized by Nanosecond Electron Microscopy, Lawrence Livermore National Laboratory (LLNL), Livermore, CA, 2005.
[53] P. Dang, M. Grujicic, An atomistic simulation study of the effect of crystal defects on the martensitic transformation in Ti - V bcc alloys, Model. Simulat. Mater. Sci. Eng. 4 (1996) 123, https://doi.org/10.1088/0965-0393/4/2/001.
[54] C. Cayron, Angular distortive matrices of phase transitions in the fcc–bcc–hcp system, Acta Mater. 111 (2016) 417–441.
[55] J.R. Morris, K.M. Ho, Molecular dynamic simulation of a homogeneous bcc -> hcp transition, Phys. Rev. B 63 (2001), https://doi.org/10.1103/PhysRevB.63.224116.
[56] D. Srivastava, S. Banerjee, S. Ranganathan, The crystallography of the BCC to HCP (orthohexagonal) martensitic transformation in dilute Zr-Nb alloys: Part I: lattice strain and lattice invariant shear, Trans. Indian Inst. Met. 57 (2004) 205–223.
[57] Q. Yu, J. Kacher, C. Gammer, R. Traylor, A. Samanta, Z. Yang, A.M. Minor, In situ TEM observation of FCC Ti formation at elevated temperatures, Scripta Mater. 140 (2017) 9–12, https://doi.org/10.1016/j.scriptamat.2017.06.033.
[58] H. Zhao, X. Hu, M. Song, S. Ni, Mechanisms for deformation induced hexagonal close-packed structure to face-centered cubic structure transformation in zirconium, Scripta Mater. 132 (2017) 63–67, https://doi.org/10.1016/j.scriptamat.2017.01.034.
[59] H. Zhao, M. Song, S. Ni, S. Shao, J. Wang, X. Liao, Atomic-scale understanding of stress-induced phase transformation in cold-rolled Hf, Acta Mater. 131 (2017) 271–279, https://doi.org/10.1016/j.actamat.2017.03.058.
[60] D.H. Hong, T.W. Lee, S.H. Lim, W.Y. Kim, S.K. Hwang, Stress-induced hexagonal close-packed to face-centered cubic phase transformation in commercial-purity titanium under cryogenic plane-strain compression, Scripta Mater. 69 (2013) 405–408, https://doi.org/10.1016/j.scriptamat.2013.05.038.
[61] M. An, Q. Deng, Y. Li, H. Song, M. Su, J. Cai, Molecular dynamics study of tension-compression asymmetry of nanocrystal α-Ti with stacking fault, Mater. Des. 127 (2017) 204–214, https://doi.org/10.1016/j.matdes.2017.04.076.
[62] X. Hu, H. Zhao, S. Ni, M. Song, Grain refinement and phase transition of commercial pure zirconium processed by cold rolling, Mater. Char. 129 (2017) 149–155, https://doi.org/10.1016/j.matchar.2017.04.037.
[63] H.C. Wu, A. Kumar, J. Wang, X.F. Bi, C.N. Tomé, Z. Zhang, S.X. Mao, Rolling-induced face centered cubic titanium in hexagonal close packed titanium at room temperature, Sci. Rep. 6 (2016) srep24370, https://doi.org/10.1038/srep24370.
[64] J.X. Yang, H.L. Zhao, H.R. Gong, M. Song, Q.Q. Ren, Proposed mechanism of HCP → FCC phase transition in titianium through first principles calculation and experiments, Sci. Rep. 8 (2018) 1992, https://doi.org/10.1038/s41598-018-20257-9.
[65] B. Li, E. Ma, Atomic shuffling dominated mechanism for deformation twinning in magnesium, Phys. Rev. Lett. 103 (2009), 035503, https://doi.org/10.1103/PhysRevLett.103.035503.
[66] B. Li, X.Y. Zhang, Global strain generated by shuffling-dominated {101-2}<10-1-1> twinning, Scripta Mater. 71 (2014) 45–48, https://doi.org/10.1016/j.scriptamat.2013.10.002.
[67] M.J. Mehl, D.A. Papaconstantopoulos, Tight-binding study of high-pressure phase transitions in titanium: alpha to omega and beyond, Europhys. Lett. 60 (2002) 248, https://doi.org/10.1209/epl/i2002-00356-y.
[68] C. Kittel, Others, Introduction to Solid State Physics, Wiley, New York, 1976.
[69] Y.-M. Kim, B.-J. Lee, M.I. Baskes, Modified embedded-atom method interatomic potentials for Ti and Zr, Phys. Rev. B 74 (2006), https://doi.org/10.1103/PhysRevB.74.014101.
[70] M.I. Baskes, R.A. Johnson, Modified embedded atom potentials for HCP metals, Model. Simulat. Mater. Sci. Eng. 2 (1994) 147, https://doi.org/10.1088/0965-0393/2/1/011.
[71] R.G. Hennig, T.J. Lenosky, D.R. Trinkle, S.P. Rudin, J.W. Wilkins, Classical potential describes martensitic phase transformations between the α , β , and ω titanium phases, Phys. Rev. B 78 (2008), https://doi.org/10.1103/PhysRevB.78.054121.
[72] J.S. Gibson, S.G. Srinivasan, M.I. Baskes, R.E. Miller, A.K. Wilson, A multi-state modified embedded atom method potential for titanium, Model. Simulat. Mater. Sci. Eng. 25 (2017), https://doi.org/10.1088/1361-651X/25/1/015010, 015010.
[73] D. Porezag, M.R. Pederson, A.Y. Liu, The accuracy of the pseudopotential approximation within density-functional theory, Phys. Status Solidi 217 (2000) 219–230, https://doi.org/10.1002/(SICI)1521-3951(200001)217:1<219::AID-PSSB219>3.0.CO;2-V.
[74] X.Y. Zhang, B. Li, J. Tu, Q. Sun, Q. Liu, Non-classical twinning behavior in dynamically deformed cobalt, Materials Research Letters 3 (2015) 142–148, https://doi.org/10.1080/21663831.2015.1034297.
[75] C.D. Barrett, H. El Kadiri, The roles of grain boundary dislocations and disclinations in the nucleation of {10-12} twinning, Acta Mater. 63 (2014) 1–15, https://doi.org/10.1016/j.actamat.2013.09.012.